Plasmonics (2022) 17:2075–2087
https://doi.org/10.1007/s11468-022-01691-y

Enhanced Sensitivity of Open Channel SPR-Based PCF Sensor Employing Plasmonic Materials for Analyte Sensing

Nazrul Islam[1] · Md. Mohi Uddin Masum[2] · Md. Faizul Huq Arif[3] · Sayed Asaduzzaman[4,5] · Monoranjon Roy[2] · Mohammad Abu Yousuf[1]

Received: 6 April 2022 / Accepted: 26 July 2022 / Published online: 18 August 2022

Abstract

Highly sensitive photonic crystal fiber (PCF) sensors based on the spectacle of surface plasmonic resonance (SPR) are analyzed numerically and demonstrated. The finite element method (FEM) technique is used to examine detection performance. This study, an SPR-based PCF structure, has been proposed which achieved a maximum amplitude sensitivity of 573.83 RIU^{-1} and wavelength sensitivity of 6000 nm/RIU at refractive index (RI) of 1.39. Plasmonic materials such as gold (Au) and titanium dioxide (TiO_2) have been implied inside the open channels of the PCF as a thin layer. The study explores different types of effects of detecting variation of gold thickness. The work also uses the simple appearance of air holes and pitch variation to achieve the best level detection performance. Moreover, a simplified geometry of SPR-based PCF has been proposed to trim the complexity of the manufacturing process. With an improved sensitivity performance, the benefit of the sensor will also make promising progress towards the detection of unknown biological analyte.

Keywords Surface plasmon resonance · Plasmonic materials · Amplitude sensitivity · Confinement loss

Introduction

SPR is a technique that is characterized as the excitation of free electron density oscillations within the metallic dielectric interface. SPR sensors are used extensively because of their high sensitivity, real-time biochemical detection capabilities, and unlabelled monitoring potentiality [1, 2]. Wide range of applications of SPR sensor has already been experienced in real life, including bio-detection, environmental monitoring, food safety, medical diagnostics, temperature sensing, strain sensing, detection of gases, and water testing [3–6]. Typically, a prism is used to excite surface plasmon. However, detection technology based on traditional prism has some drawback as enormous in area and cost in price [7]. In addition, prism-based SPR detection technology is not suitable for miniaturization and bio-sensing applications [8]. Such disadvantages can be overcome by using a lens as a prism substitute.

Highlights

1. A maximum amplitude sensitivity of 573.83 RIU^{-1} and wavelength sensitivity of 6000 nm/RIU at Refractive Index (RI) of 1.39.
2. The research explores different types of effects of detecting variation of gold thickness.
3. The maximum peak loss in Y axis is 377.21 (dB/cm) because of the open channel in the Y direction with RI between 1.33 and 1.40.

✉ Nazrul Islam
nazrul.islam@ieee.org

✉ Sayed Asaduzzaman
s.asaduzzaman@rmstu.edu.bd

Md. Mohi Uddin Masum
masum.mbstu@gmail.com

Md. Faizul Huq Arif
arifict27@gmail.com

Monoranjon Roy
monoranjonroy.mr@gmail.com

Mohammad Abu Yousuf
yousuf@juniv.edu

[1] Institute of Information Technology (IIT), Jahangirnagar University, Dhaka 1342, Bangladesh

[2] Department of Information and Communication Technology, Mawlana Bhashani Science and Technology University, Tangail 1902, Bangladesh

[3] Department of ICT (DoICT), Information and Communication Technology (ICT) Division, Government of the People's Republic of Bangladesh, Dhaka, Bangladesh

[4] Department of Computer Science and Engineering, Rangamati Science and Technology University, Rangamati, Bangladesh

[5] Department of Computer Science and Engineering, Daffodil International University, Dhaka, Bangladesh

In 1993, Jorgenson and Yee [9] highlighted a first optical fiber technology-based SPR sensor. The invention of the PCF opened a new window by removing the limitations of conventional optical fiber. PCFs are also known as microstructured fiber optics which have attracted the attention of researchers for its diversity of real-world applications. In comparison to conventional fiber optics, PCF embraces more flexible design structures. It also exhibits high sensitivity, lower electromagnetic interference, configurable birefringence, single mode propagation, and high confinement loss [10]. In 2006, the first SPR sensor based on PCFs was developed by Hassani and Skorobogatiy [11]. There are many PCF structures that were introduced with gold (Au) and silver (Ag) as plasmonic metal due to their stability and resonance change [12]. However, it has also been reported that plasmonic materials titanium dioxide (TiO_2) layer outside the gold (Au) or silver (Ag) film can enhance the performance of SPR sensor significantly [13].

There are two kinds of PCF sensor detection approaches based on SPR which are internally and externally detected. In the internal detection method, the detection channels are formed inside the PCF by filling the air outlets with analyte. On the contrary, in the external sensing mechanism, analyte directly contracts the outer layer of the fiber. There has been extensive research on different structural parameters of SPR-based sensor PCF. The research [14] shows a double SPR-PCF core coated with gold and air holes are located hexagonaly. This study found the highest amplitude sensitivity (AS) of 1770 RIU^{-1} and wavelength sensitivity (WS) of 10,700 nm/RIU within refractive index (RI) between 1.39 and 1.40. According to [15], the authors used plasmonic material, for example, gold, where the hightest wavelength sensitivity of 21,200 nm/RIU and resolution of 4.72×10^{-6} RIU^{-1}. This work could be performed in biochemical sensing applications.

In addition, the work [16] proposed an SPR-based PCF employing gold (Au) that was analyzed and studied numerically. The authors observed a maximum WS of 10,000 nm/RIU and an AS of 1250 RIU^{-1}. The sensor provides enhanced performance for various biochemical and RI between 1.33 and 1.39. As well, in another paper [17], a highly sensitive state of being calibrated based on SPR was suggested. Two polarized modes have been used to find high sensitivity where structural parameters are optimized. As well, the sensor detected a WS of 6700 nm/RIU as well as resolution of 10,000 nm/RIU. The self-calibrated sensor is highly accurate and linear. The research [19] highlighted a numerical analysis of a hollow ring-shaped SPR-PCF. The sensor uses silver as the plasmonic material for external sensing and more practical application. It also obtained a WS of 21,000 nm/RIU and an AS of 2456 RIU^{-1}. As well, the wavelength resolution achieved 4.76×10^{-6} RIU and the amplitude resolution was 4.07×10^{-6} RIU within RI range is between 1.33 and 1.42.

Moreover, in the work [20], a double-core PCF was proposed with a hexagonal lattice frame. The numerical study demonstrates that the structure reached a WS of 21,679 nm/RIU and 22,983 nm/RIU for RI value of 1.33 and 1.43 reported correspondingly. Another work [21] proposed a hexagonal geometric structure of SPR-based PCF sensor with gold coating which obtains the top-notch WS of 3000 nm/RIU and the spectral resolution of 13,000 nm/RIU within RI is from 1.33 to 1.37. Furthermore, the authors [22] introduce a square mesh shape to increase the significant performance of the SPR which has two active layers of plasmonic materials gold is legible on the interior surface of both channel. Here, the maximum WS of 6300 nm/RIU is reported; the RI value is 1–1.43.

The proposed work is designed with an SPR-based PCF with gold (Au) coating and titanium dioxide (TiO_2) with two open channels and follows the external sensing method. The appropriate optimization and structural parameters, for example, air hole diameters, ellipticity, layer thickness of Au and TiO_2, and the radius of open channels, have been discussed in detail. The efficiency of the proposed sensor has also been analyzed for the optimized structural parameters. It is further noted that as required by the analyte, the open channel radius can be adapted.

Structural Design and Theory

The proposed design aims to enable the optical signal to escape from the core to the metallic dielectric layer. The escaped signal creates a surface plasma wave (SPW) which speeds up the oscillation of electrons in the metal. The incident light of the frequency is aligned to the oscillatory frequency of the associated electrons. The maximum energy is coupled to the free electrons, which is known as surface plasmon polarizations (SPP). For certain wavelengths, the central guided mode is SPP mode.

There are three air holes that are defined as large air holes (d_1), middle air holes (d_2), and small air holes (d_3). Gold layer thickness is denoted by t_g, titanium dioxide (TiO_2) thickness is presented by t_t, elliptic air holes is symbolized by e, and open channel radius is defined as r. The structure of the PCF is simulated several times at different values where other parameters are constant using this process to optimize the value of the parameters. After optimization, the values of the parameters are $\lambda = 2.05$ µm, $r = 2.4$ µm, $d_1 = 55$ µm, $d_2 = 42$ µm, and $d_3 = 30$ µm. The thicknesses of gold (Au) and TiO2 are $t_g = 40$ nm and $t_t = 40$ nm, as a consequence. The eccentricity between the two elliptic air holes is $e = 0.44$.

The cross-section view of the proposed PCF is illustrated in Fig. 1. The structure has three sections. The internal part of the structure is silica, which is arranged with 16 circular air holes and 2 elliptical. The remaining two layers of the grid are the sheet metal and the analyte layer. Typically, gold, copper, silver, and aluminum are practiced as plasmonic materials in existing research. However, among plasmonics, gold (Au) has a chemically stable behavior. As well, gold (Au) responds with a higher resonant peak. Thus, in this work, the gold layer (Au) is used to enclose the coating section of the sensor structure. A narrow coating of titanium dioxide (TiO_2) is utilized in the middle of the fiber. This TiO_2 layer improves the interplay of analysts and plasmons. The outermost part of the structure has a perfectly matched layer (PML) that is included to reduce unwanted non-physical emission to the surface.

Fused silica (SiO_2) is practiced as a fundamental material and RI (n) for silica is acquired in the Sellmeier dispersion calculation below [23].

$$n^2(\lambda) = 1 + \frac{B_1\lambda^2}{\lambda^2 - C_1} + \frac{B_2\lambda^2}{\lambda^2 - C_2} + \frac{B_3\lambda^2}{\lambda^2 - C_3} \quad (1)$$

where n symbolizes pure silica of RI, which depends on different wavelengths λ. Additionally, B_1, B_2, B_3, C_1, C_2, and C_3 represent the values of Sellmeier constants. The constant value is B_1=0.69616300, B_2=0.407942600, B_3=0.89779400, C_1=0.00467914826 μm^2, C_2=0.0135120631 μm^2, and C_3 =97.9340025, μm^2 accordingly.

The permittivity of gold (Au) can be found from the following relation [24].

$$\varepsilon_{Au} = \varepsilon_\infty - \frac{\omega_D^2}{\omega(\omega + j\gamma_D)} - \frac{\Delta\varepsilon.\Omega_L^2}{(\omega^2 - \Omega_L^2) + j\Gamma_L\omega} \quad (2)$$

Here, gold (Au) permittivity is presented by ε_{Au}, and the high frequency of permittivity denotes $\varepsilon_\infty = 5.9673$. And $\omega = 2\pi c/\lambda$ indicates angular frequency, c is the velocity of light in a vacuum, γ_D denotes the frequency of damping (15.92 THz). Similarly, ω_D represents the frequency of plasma (2113.6 THz). The Lorentz oscillators weighting factor $\Delta\varepsilon = 1.09$. The spectral width and oscillator strength of the Lorentz oscillators are expressed by $\Gamma_L/2\pi = 104.86$ THz and $\Omega_L/2 = 650.07$ THz, accordingly.

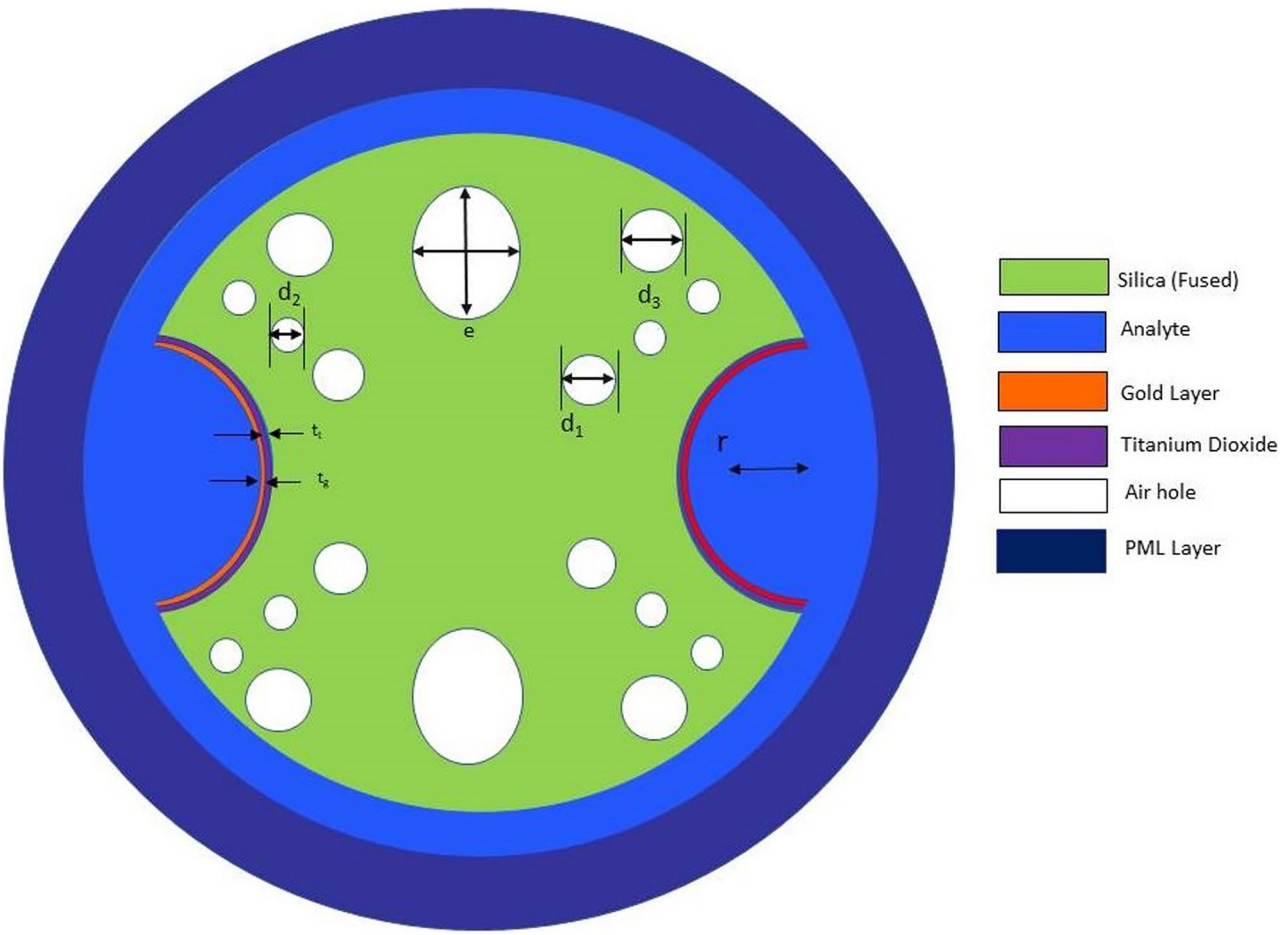

Fig. 1 Slice view of the proposed SPR-PCF probe

The RI of TiO_2 is calculated using the formula [25].

$$n_t = \sqrt{5.913 + \frac{2.441 \times 10^7}{\lambda^2 - 0.803 \times 10^7}} \quad (3)$$

Here, n_t denotes titanium dioxide RI and λ represents wavelength.

The proposed sensor was configured in the approach such that the stack and pull method could be used to assemble the fiber structure. The guiding cores could be created by replacing capillaries with solid rods. However, depositing a uniform Au and TiO_2 layer is a challenging task inside the open channels of the PCF. In this case, high-pressure microfluidic chemical deposition, wheel polishing, and atomic layer deposition (ALD) techniques are suitable to cover the surface with a decorative layer, the PCF with narrow gold (Au) and titanium dioxide (TiO_2) layers [26].

The COMSOL Multiphysics version 5.3a tool makes it possible to study the propagation mode of the sensor using the finite element method (FEM). Appropriate boundary conditions are provided to confine backscatter with a PML, which was taken 0.85 µm thick following the convergence test. The thickness of the layer to be analyzed is 0.45 µm when the simulation is performed. The results showed that the mesh components deviated considerably from the respective guided modes. A greater mesh size produces a decreasing number of triangular components that consume comparatively less time and can produce inappropriate outcomes. According to the theory, a suitable mesh size is used to obtain reliable results.

Result and Numerical Analysis

Coupling Properties

The basic mode of the *x*- and *y*-polarized distribution of electric field is shown in Fig. 2a, b accordingly. It can also be seen from the figures that the central mode is almost limited in the central area. Figure 2c presents the electric field distribution in SPP mode. Furthermore, the plasmonic mode is allocated between the metallic layers (Au, TiO_2) and the analyte layer. Additionally, coupling improved the signal simply propagated at the resonant wavelength between SPP mode and core mode.

Figure 3 illustrates the resonance condition for loss spectrum, SPP mode, and core mode according to wavelength. The figure clearly shows that the actual portion of the RI for core mode and SPP mode is identical to the wavelength of 0.74 µm. At this stage, the wavelength is referred to as the resonating wavelength. At the same point, confinement loss reaches its peak. More confinement loss leads to a more evanescent field within the coating area, which enhances sensitivity.

Confinement loss can be defined as [27].

$$\alpha_{loss} = 8.686 k_0 Im(n_{eff}) \times 10^4 (\mathrm{dB/cm})$$

Here, $Im(n_{eff})$ indicates RI imaginary part and wave number is represented by $k_0 = 2\pi/\lambda$, whereas λ symbolizes the input light wavelength. A high-sensitivity PCF sensor should be able to detect very little variation of RI. A small variation in the RI is easily detectable. $Im(n_{eff})$ may be affected by the RI analyte (n_a). It is displayed in Fig. 4a, which contains the analyte (n_a) between 1.33 and 1.40. From Fig. 4a, it is found a minimum confinement loss (CL) of 47.08 (dB/cm) at λ= 0.61 µm and n_a = 1.33. Besides, the maximum loss occurs at λ = 0.80 µm and the value is 377.21 (dB/cm) for n_a = 1.40.

Wavelength and Amplitude Sensitivities

Sensitivity is the key indicator for estimating sensor performance. In order to measure the values of wavelength sensitivity, generally, the wavelength interrogation approach is used. The wavelength interrogation equation is defined as [28].

$$S_\lambda = \Delta\lambda_{peak}/\Delta n_a \ (\mathrm{nm/RIU})$$

Here, $\Delta\lambda_{peak}$ indicates displacement of resonant wavelength. The symbol Δn_a indicates changes of RI. However, the wavelength sensitivity is expensive and difficult to implement since the technique of interrogating the wavelengths is associated with the spectral manipulation. On the contrary, in the amplitude interrogation approach,

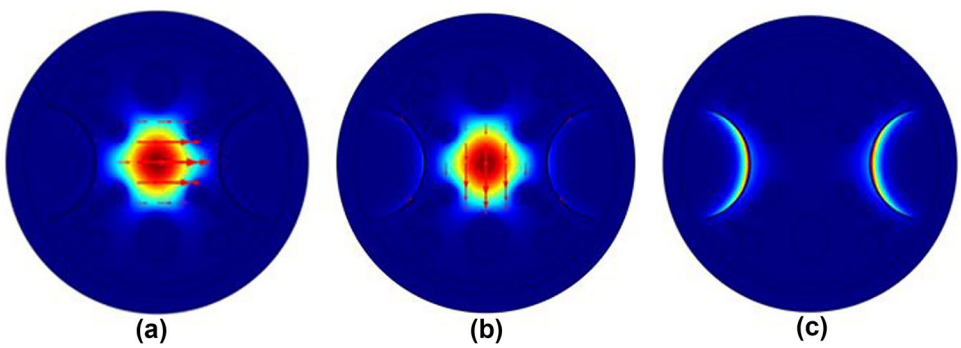

Fig. 2 Distribution of electric field: **a** *x*-polarized core mode, **b** *y*-polarized core mode, and **c** *y*-polarized plasmonic mode at Λ = 0.74 µm, RI = 1.39, and other parameters remained the same at Λ = 2.05 µm, d_1 = 55 µm, d_2 = 42 µm, d_3 = 20 µm, t_g = 40 nm, t_t = 40 nm, r = 2.4 µm, and e = 0.44 µm

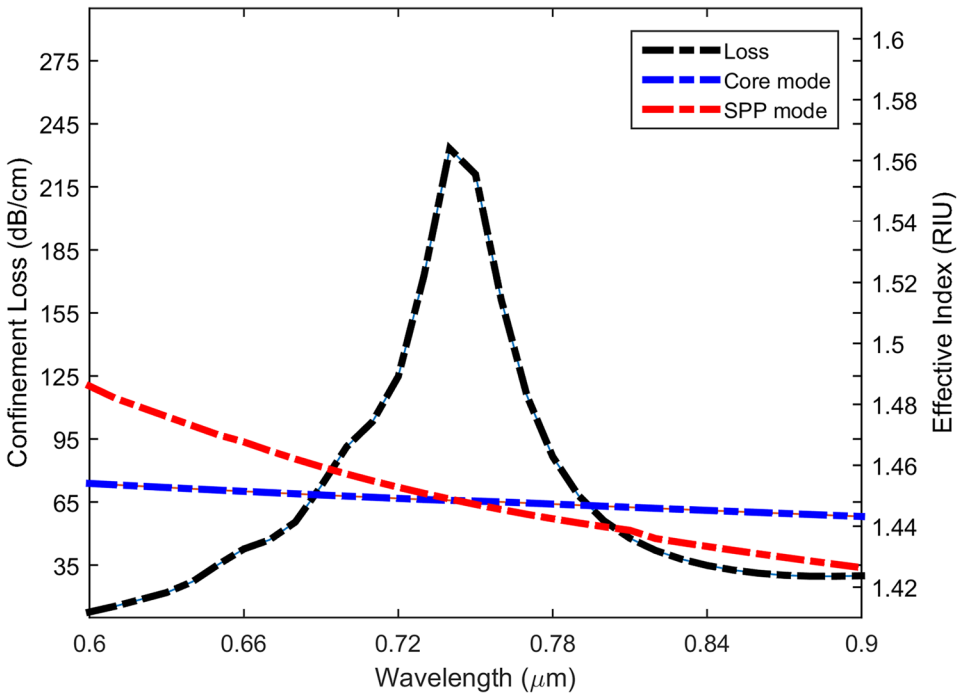

Fig. 3 Situation from the occurring condition of resonance with other parameters is fixed at $\Lambda = 2.05$ µm, $d_1 = 55$ µm, $d_2 = 42$ µm, $d_3 = 20$ µm, $t_g = 40$ nm, $t_t = 40$ nm, $r = 2.4$ µm, and $e = 0.44$ µm

spectral manipulation is not needed. Consequently, the amplitude interrogation technique becomes cost-efficient and simple. The amplitude sensitivity can be expressed as per the following relationship [29].

$$S_A = -\frac{\partial\alpha(\lambda, n_a)/\partial n_a}{\alpha(\lambda, n_a)} \left(\mathrm{RIU}^{-1}\right)$$

where $\alpha(\lambda, n_a)$ indicates the overall loss of propagation at any wavelength and $\partial\alpha(\lambda, n_a)$ signifies the loss differently.

Figure 4b distinctly demonstrates that using the optimum design parameter, the highest peak amplitude sensitivity is found 573.83 RIU^{-1} at a wavelength of 0.74 µm for the value of $n_a = 1.39$. Figure 4b illustrates the amplitude sensitivity spectrum for the variation of n_a between 1.33 and 1.39.

For further details, n_a of 1.33, 1.34, 1.35, 1.36, 1.37, 1.38, and 1.39 have corresponding maximum amplitude sensitivities 71.71, 93.57, 108.26, 131.99, 195.35, 311.04, and 573.83 RIU^{-1} correspondingly. Besides, a maximum

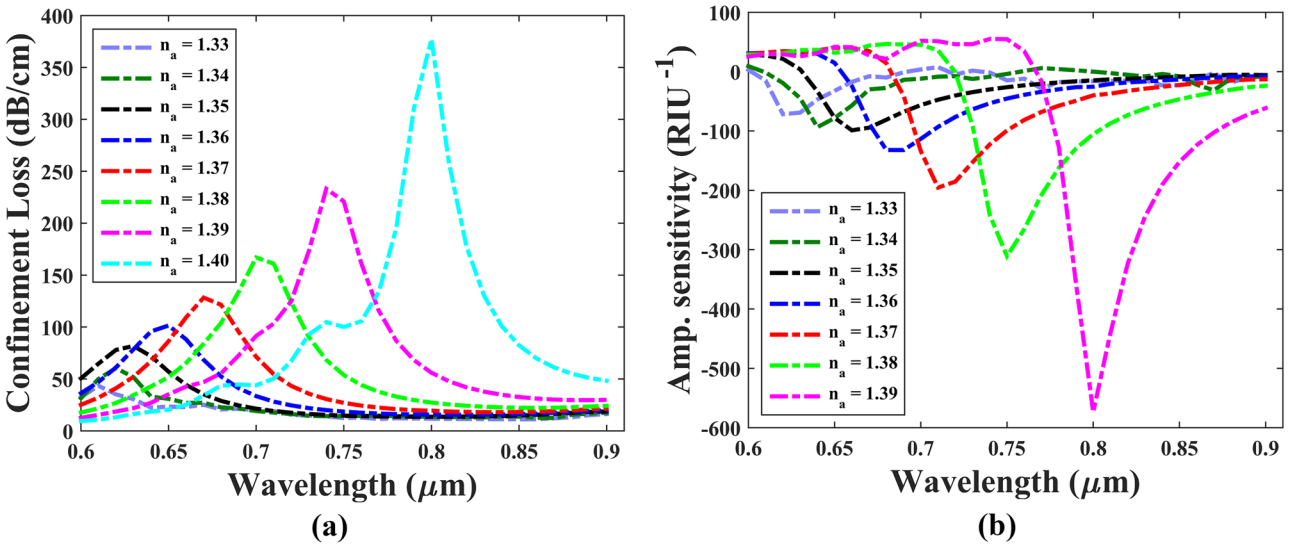

Fig. 4 Changes in **a** loss spectrum and **b** AS within analyte RI vary between 1.33 and 1.39. Another parameters are fixed at $\Lambda = 2.05$ µm, $d_1 = 55$ µm, $d_2 = 42$ µm, $d_3 = 20$ µm, $t_g = 40$ nm, $r = 2.4$ µm, and $e = 0.44$ µm

Table 1 Sensor performance comparison of wavelength sensitivity, sensor resolution, and amplitude sensitivity by changing the values of n_a from 1.33 to 1.40

n_a	Δn_a	Peak loss (dB/cm)	λ_{peak} (nm)	$\Delta\lambda_{peak}$ (nm)	S_λ (nm/RIU)	R (RIU)	S_A (RIU^{-1})
1.33	0.01	47.08	610	10	1000	1×10^{-4}	71.71
1.34	0.01	60.43	620	10	1000	1×10^{-4}	93.57
1.35	0.01	74.72	630	20	2000	5×10^{-5}	108.26
1.36	0.01	101.44	650	20	2000	5×10^{-5}	131.99
1.37	0.01	128.35	670	30	3000	3.33×10^{-5}	195.35
1.38	0.01	166.99	700	40	4000	2.5×10^{-5}	311.04
1.39	0.01	233.13	740	60	6000	1.6×10^{-5}	573.83
1.40	0.01	377.21	800	-	-	-	-

resolution of 1.6×10^{-5} RIU is reached at the RI about 1.39. The scenario of WS, resolution, and AS has been displayed in Table 1 for different analyte RI from 1.33 to 1.40.

Effect of Gold (t_g) and TiO2 (t_t) Thicknesses on Sensor Performance

Figure 5 shows the effect on the detection performance for the variation of the thickness of gold (Au). Here, gold (Au) thickness values go from 35 to 45 nm with a range of 5 nm for n_a of 1.39 and 1.40. In Fig. 5, the CL decreases with a thick gold film (Au) whereas CL rises with thinner gold (Au). From Fig. 5a, the sensor is observed to have a maximum confinement loss of 475.43 dB/cm approximately for t_g of 35 nm with the RI analyte of ($n_a=1.40$). The larger the thickness of the gold film, the greater the reduction in peak loss. The variation in AS is given in Fig. 5b, for different gold (Au) layer thicknesses. It is found that an AS of approximately 611.68 RIU^{-1}, 573.83 RIU^{-1}, and 413.59 RIU^{-1} for t_g value are 35 nm, 40 nm, and 45 nm respectively. A thin TiO_2 layer after gold layer has been added. The analysis of the TiO_2 film thickness (t_t) is presented in Fig. 6.

Figure 6a demonstrates that confinement loss as a wavelength function with varying thicknesses of titanium dioxide ($t_t=35$ nm, 40 nm, and 45 nm). With $t_t=35$ nm thickness of the titanium dioxide coating (TiO_2), the confinement loss proved greater than the 40 nm thickness. Furthermore, a thickness of 40 nm results in a loss exceeding a thickness of 45 nm. The thickness $t_t=35$ nm indicates a maximum loss of 151.4 dB/cm at a wavelength of 0.82 μm. The thickness $t_t=40$ nm shows a confinement loss of 87.54 dB/cm with wavelength of 0.81 μm. The thickness $t_t=45$ nm shows the lowest peak that produces confinement loss of 56.48 dB/cm with wavelength of 0.82 μm. Figure 6b shows the highest AS for $n_a=1.39$ with $t_t=35$ nm.

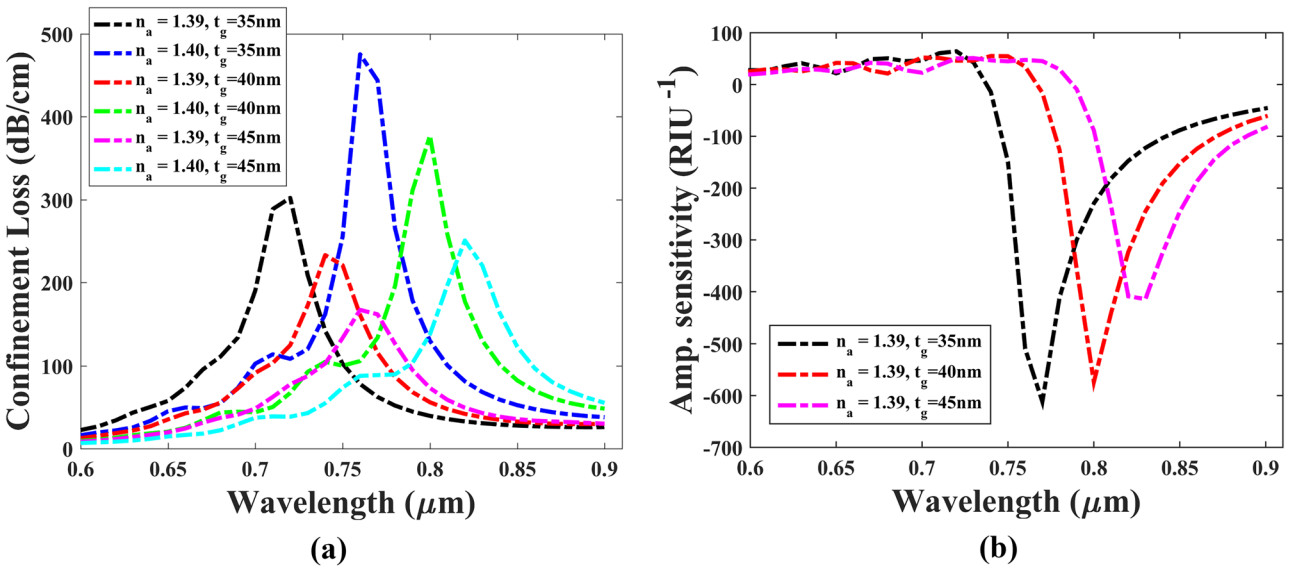

Fig. 5 Variation of **a** curves of CL with RI of $n_a=1.39$ and 1.40 for different values of gold (Au) thickness ($t_g=35$ nm, 40 nm, and 45 nm) and **b** AS for $t_g=35$ nm, 40 nm, and 45 nm at analyte RI of $n_a=1.39$; other parameters remain the same at $\Lambda=2.05$ μm, $d_1=55$ μm, $d_2=42$ μm, $d_3=20$ μm, $r=2.4$ μm, and $e=0.44$ μm

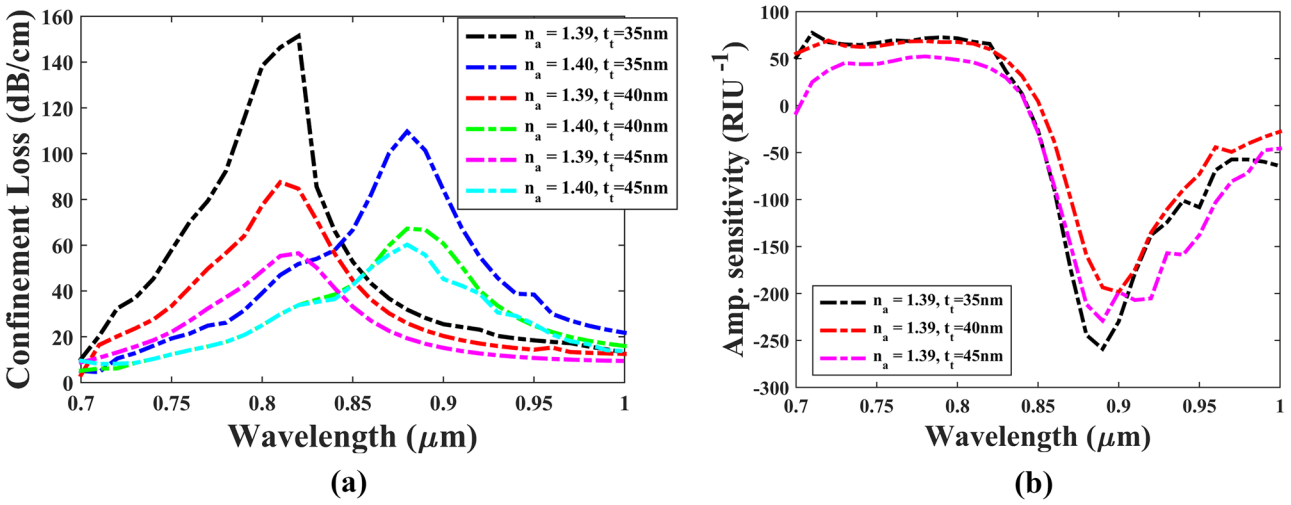

Fig. 6 Changes of **a** loss spectrum at analyte RI of $n_a = 1.39$ and 1.40 for different TiO_2 layer thicknesses of $t_t = 35$ nm, 40 nm, and 45 nm, and **b** amplitude sensitivity curves for of $t_t = 35$ nm, 40 nm, and 45 nm at analyte RI of $n_a = 1.39$

Effect of Larger Air Hole Diameter (d_1) on Sensor Performance

The size of the air hole impacts the core mode's refractive index (RI), which also matches the SPP mode. It demonstrates the effect of the change in the diameter (d_1) of the air holes near the central area on the confinement loss and sensor's amplitude sensitivity. Besides, it is observed from Fig. 7a that the value of d_1 increases, and the confinement loss is increased. The spectrum of confinement loss (CL) and the scenario of amplitude sensitivity for d_1 of 45 µm, 50 µm, and 55 µm are shown in Fig. 7b. Also, it can be seen that there are no significant changes for the change in d_1.

Effect of Middle Air Hole Diameter (d_2) on Sensor Performance

The effects of variation in the diameter of average air holes (d_2) away from the central area were also analyzed. Figure 8a shows that lower value of d_2 results in increased confinement loss. In Fig. 8b, there is no significant effect to change the values of d_2 in terms of sensitivity. However, it is seen that

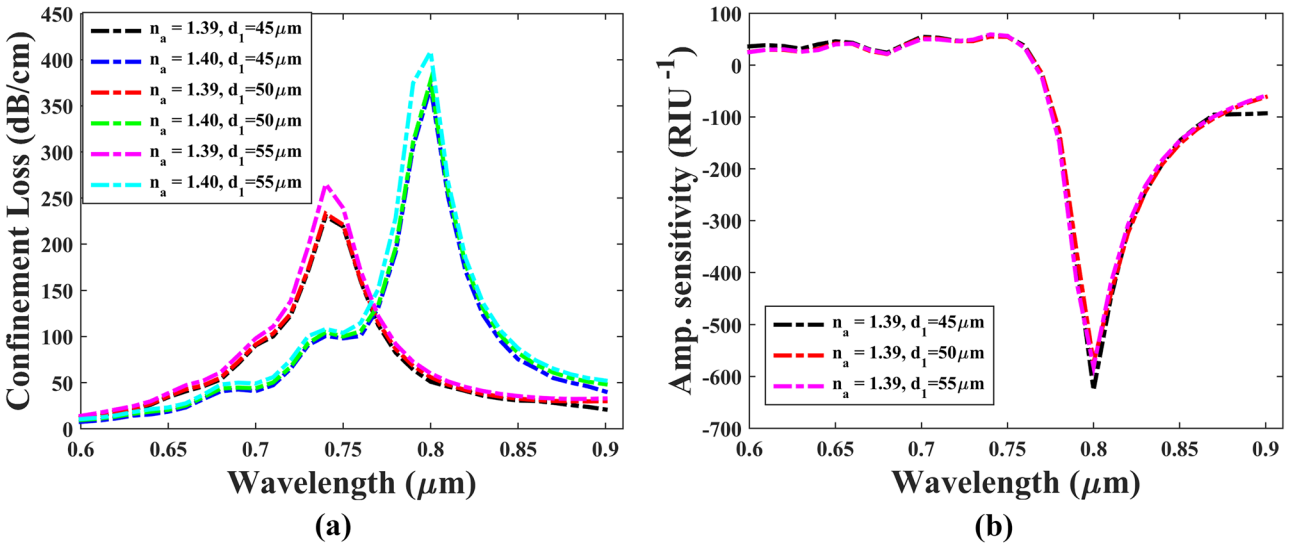

Fig. 7 Changes of **a** confinement loss (CL) spectrum for $d_1 = 45$ µm, 50 µm, and 55 µm at RI of $n_a = 1.39$ and 1.40, and **b** AS values $d_1 = 45$ µm, 50 µm, and 55 µm at RI of $n_a = 1.39$; other parameters remained the same at $\Lambda = 2.05$, $d_2 = 42$ µm, $d_3 = 20$ µm, $r = 2.4$ µm, $t_g = 40$ nm, $t_t = 40$ nm, and $e = 0.44$ µm

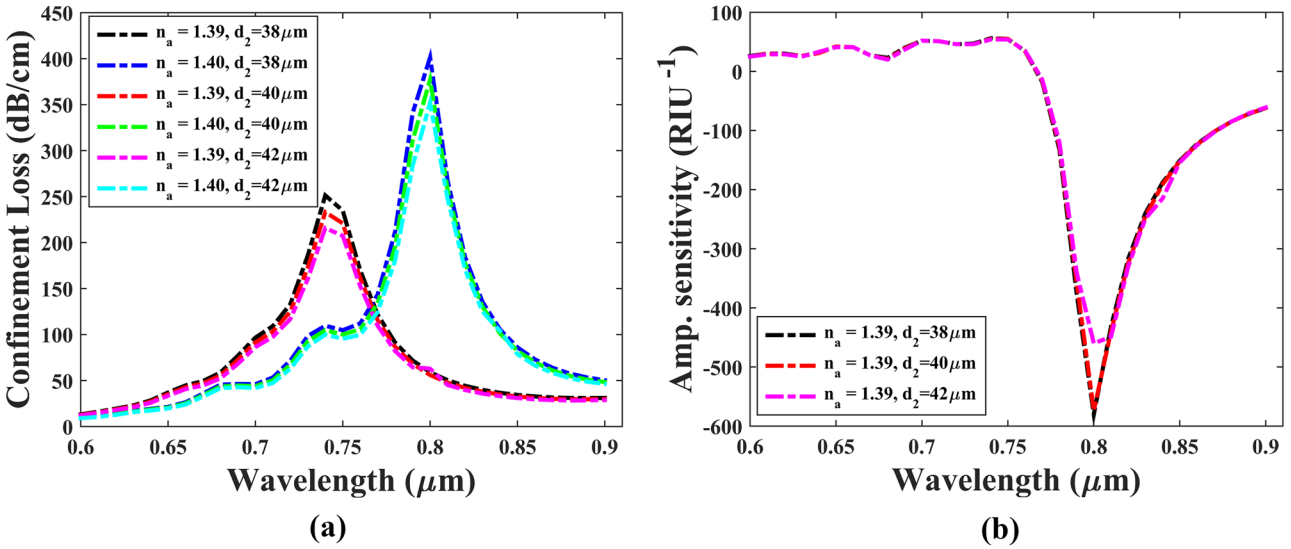

Fig. 8 Variation of **a** confinement loss for $d_2 = 38$ µm, 40 µm, and 42 µm with RI value between 1.39 and 1.40, and **b** AS values for $d_2 = 38$ µm, 40 µm, and 42 µm at RI of $n_a = 1.39$; another parameters are remaining constant at $\Lambda = 2.05$ µm, $d_1 = 55$ µm, $d_3 = 20$ µm, $r = 2.4$ µm, $t_g = 40$ nm, $t_t = 40$ nm, and $e = 0.44$ µm

higher values of d_2 show slightly higher sensitivity. Hence, $d_2 = 42$ µm is optimized for the proposed structure.

Effect of Small Air Hole Diameter (d_3) on Sensor Performance

Figure 9 shows the effects of changing the smaller size (d_3) of the air holes. It is found that lower values of d_3 indicate a lower loss of confinement and a comparatively higher sensitivity. As a result, $d_3 = 20$ µm was selected as the optimized value of the designed PCF structure.

Effect of Pitch (p) and Eccentricity (e) on Sensor Performance

The effect of changing the pitch values is illustrated in Fig. 10. It is noted that there is no significant change in height values for loss of confinement and sensitivity. However, it seems

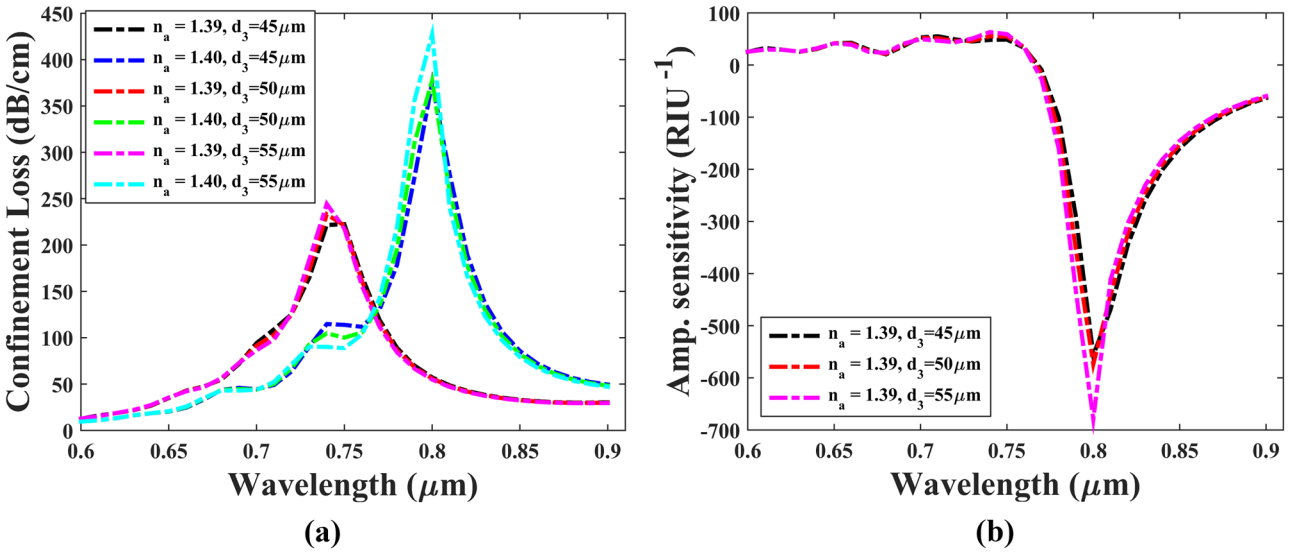

Fig. 9 Variation of **a** confinement loss for $d_3 = 20$ µm, 25 µm, and 30 µm with RI between 1.39 and 1.40, and **b** AS values for $d_3 = 20$ µm, 25 µm, and 30 µm at $n_a = 1.39$; other parameters are fixed at $\Lambda = 2.05$ µm, $d_1 = 55$ µm, $d_2 = 42$ µm, $r = 2.4$ µm, $t_g = 40$ nm, $t_t = 40$ nm, and $e = 0.44$ µm

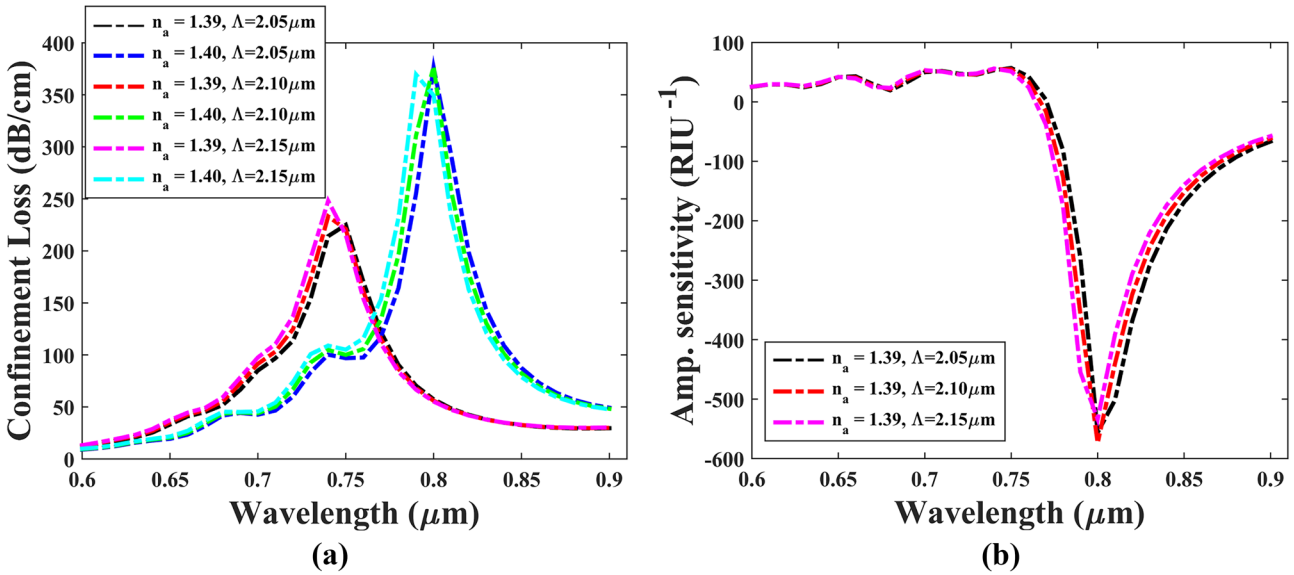

Fig. 10 Changes of **a** loss curves for different pitches of $\Lambda = 2.05$ µm, $\Lambda = 2.10$ µm, and $\Lambda = 2.15$ µm at different values of RI ($n_a = 1.39$ and 1.40), and **b** AS for $\Lambda = 2.05$ µm, $\Lambda = 2.10$ µm, and $\Lambda = 2.15$ µm at RI of $n_a = 1.39$; constant values are $d_1 = 0.45$ µm, $d_2 = 0.25$ µm, $d_3 = 0.5$ µm, $t_g = 40$ nm, $t_t = 40$ nm, $r = 2.4$ µm, and $e = 0.6$ µm

lower values of pitch shows a lower confinement loss. Hence, $\Lambda = 2.05$ µm has been selected as optimum value of pitch.

Figure 11a shows changes in the wavelength loss spectrum for different values of elliptical air hole eccentricity. It seems that the variation in eccentricity does not affect significantly on the CL curves of the PCF. However, it is observed that a higher value of eccentricity reduces the CL slightly. According to Fig. 11b, there appears to be no significant effect of the variation in eccentricity on the performance of the PCF in terms of amplitude sensitivity.

Effect of Open-Channel on Sensor Performance

Figure 12a illustrates the effect of varying the open channel radius (r). Figure 12a indicates that the diameter of the open channel is increasing from 2.35 to 2.45 µm; the

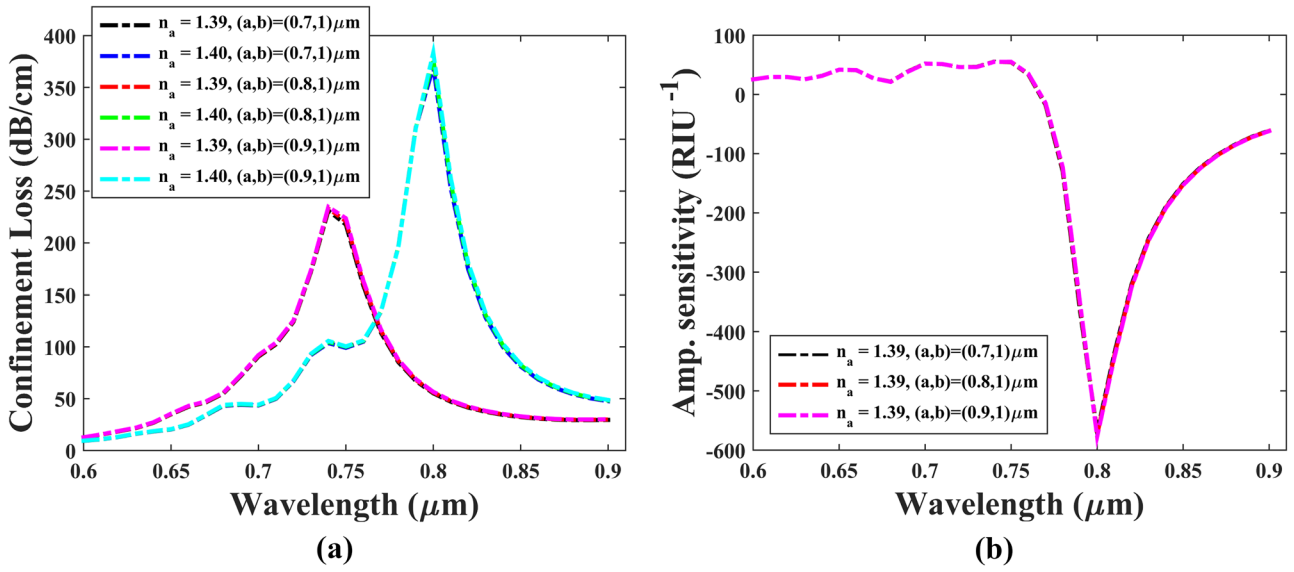

Fig. 11 Variation of **a** confinement loss (CL) for the change of eccentricity of *(a,b)* = (0.70,1), (0.80,1), and (0.90,1) and **b** amplitude sensitivity with $n_a = 1.39$, and other parameters remains the same at $\Lambda =$ 2 µm, $d_1 = 0.45$ µm, $d_2 = 0.25$ µm, $d_3 = 0.5$ µm, $t_g = 35$ nm, $t_t = 35$ nm, and $r = 2.4$ µm

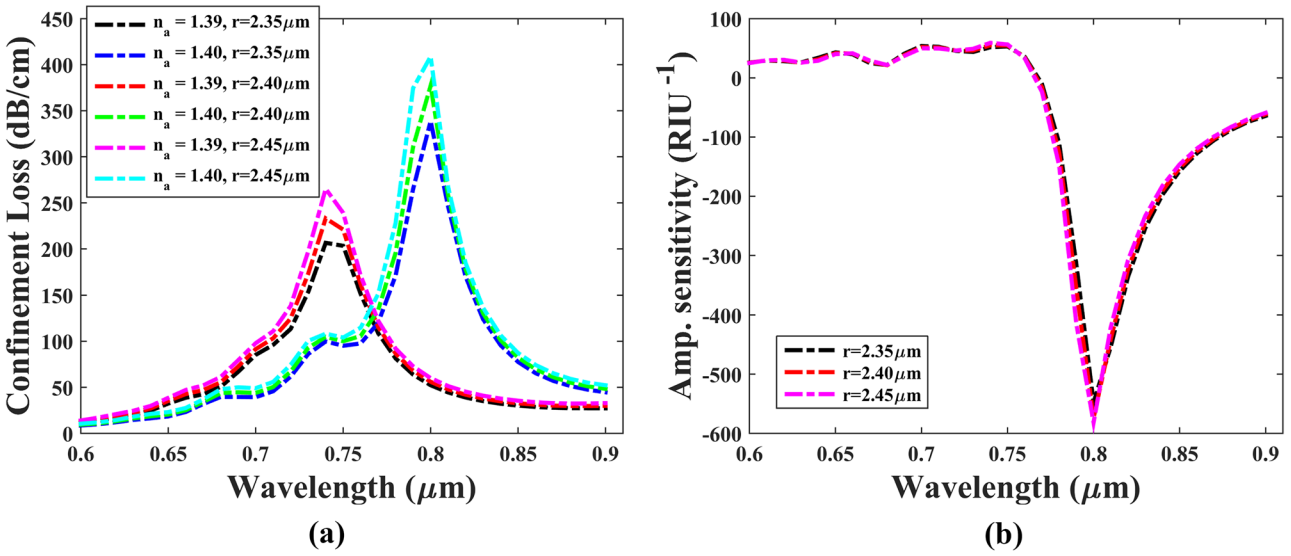

Fig. 12 **a** Loss spectrum for enlarging the radius of the open channel 2.35 μm to 2.45 μm and **b** amplitude sensitivity to changing the radius of the open channel with an analyte RI at 1.39

confinement loss is also increasing rapidly from 206.53 dB/cm to 265.23 dB/cm and 257.96 dB/cm to 408.91 dB/cm for $n_a = 1.39$ and $n_a = 1.40$ respectively. Moreover, the modification of the radius of the open channel does not have a significant impact on the amplitude sensitivity is shown in Fig. 12b. There is a slight change in the sensitivity of the amplitude of change of the radius of the open channel. Also, the amplitude sensitivity is 548, 573, and 581 RIU^{-1} for the radius of the open channel 2.35, 2.40, and 2.45 μm respectively.

This study is regarded as the 5% and 10% fabrication tolerance at its optimum values. The effects of a 5% and 10% variation of the t_g and pitch values on sensitivity are shown in Fig. 13a, where optimum value is $t_g = 40$ nm. As can be plainly seen in Fig. 13a, the difference in the thickness of the gold layer of 5% and 10% leads to a significant change in the sensitivity of the amplitude. Consequently, special attention needs to be given when depositing the gold (Au) layer on the inner surface of the open channels. Also, a variance of 5% and 10% from the pitch value has no significant effect on amplitude sensitivities as shown in Fig. 13b.

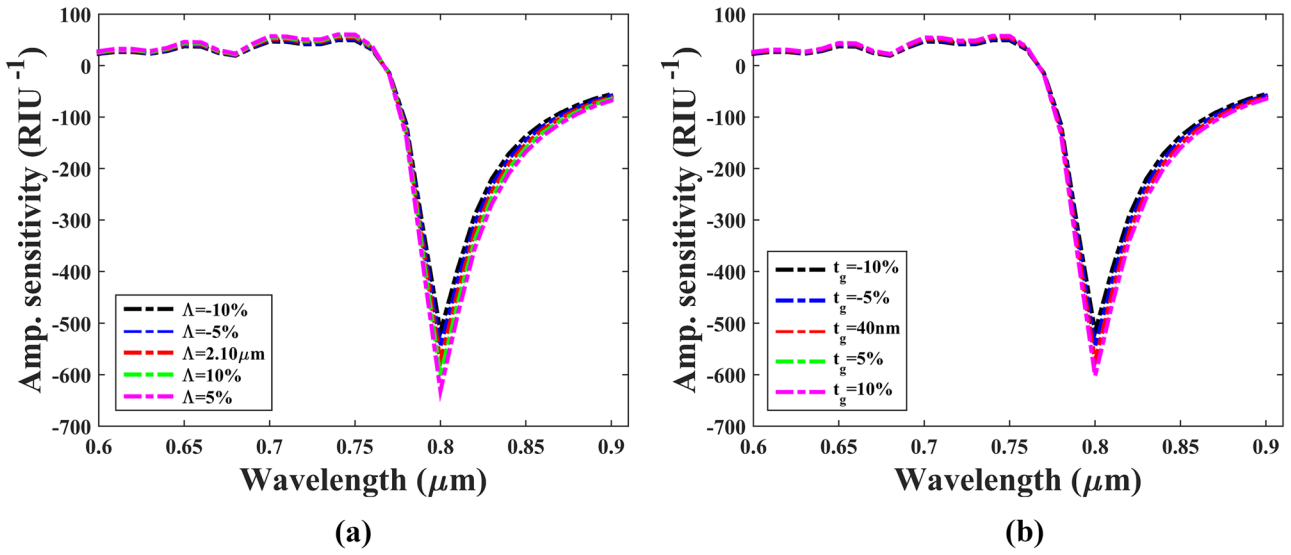

Fig. 13 **a** Fabrication tolerance due to the deviation of gold layer thickness by ± 5% and ± 10% of their optimum value and **b** fabrication tolerance due to the deviation of pitch value by ± 5% and ± 10% of their optimum value

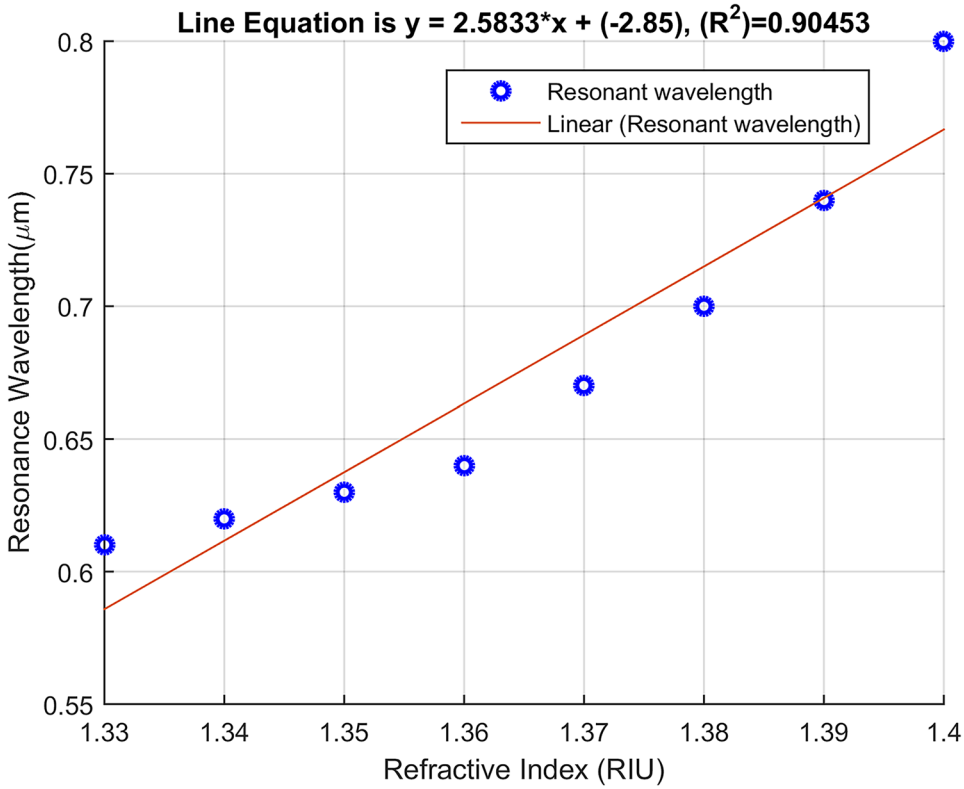

Fig. 14 Linear adjustment of the resonance wavelength to various RI of analytes from 1.33 to 1.40

Linear Curve Fitting Characteristics of the Resonance Wavelength

High linear features are a significant factor for a good sensor. Proper linear adjustment indicates the high performance accuracy of the PCF sensor. Figure 14 shows a high linearity of the suggested PCF. Moreover, it is followed that resonance wavelengths increase with increasing the analyte RI. The linear adjustment of the resonance wavelength is responsible for the equation below, while the resultant value of the linear regression of the fitted line is $R^2 = 0.9045$.

$$y = 2.5833x - 2.85$$

Here, x and y represent the RI analyte and the corresponding resonant wavelength, accordingly. Considering the entire RI range, R^2 is observed at approximately 0.90453, indicating enhanced linearity. These high linear properties are expected to be used in bio-sensing applications.

Table 2 presents a comparison to existing plasmonic sensors in terms of wavelength sensitivity, amplitude sensitivity, and resolution for different RI ranges. It is noticeably observed that the proposed PCF has an increased efficiency compared to the existing plasmonic sensors shown in Table 2.

Table 2 Comparing the efficiency between existing plasmonic sensors and the proposed sensor

Reference	Analyte RI range	Wavelength sensitivity (nm/RIU)	Amplitude sensitivity (RIU^{-1})	Resolution (RIU)
Paper work 1 [18]	1.33–1.38	5000	396	2.5×10^{-5}
Paper work 2 [30]	1.33–1.36	4000	478	2.5×10^{-5}
Paper work 3 [31]	1.33–1.37	4200	300	2.38×10^{-5}
Paper work 4 [32]	1.33–1.38	4600	371.5	2.17×10^{-5}
Paper work 5 [33]	1.44–1.46	4900	-	-
Paper work 6 [34]	1.33–1.364	3450	_	-
Proposed work	**1.33–1.39**	**6000**	**573.83**	$\mathbf{1.6\times10^{-5}}$

Conclusion

The paper proposed an SPR-based PCF and a comprehensive numerical analysis was conducted using the FEM method to detect biological analyte. This sensor is studied with many structural parameters, for example, diameter of air holes; gold and titanium dioxide (TiO2) thickness was varied and investigated. The proposed probe amplitude sensitivity is attained, 573.83 RIU^{-1}, and wavelength sensitivities are acquired 6000 (nm/RIU) with RI of 1.39. The SPP mode and the main *y*-polarization mode produce a complete coupling. The maximum peak loss in *y* axis is 377.21 (dB/cm) because of the open channel in the *y* direction with RI between 1.33 and 1.40. The proposed PCF structure is a highly sensitive biosensor with an easy-to-build structure. Additionally, due to the increased sensitivity performance, it is expected that the sensor results may potentially be applied to bio-detection applications.

Acknowledgements The authors are grateful to those who have participated in this research.

Author Contribution NI and SA: formulated the main work, designed, and wrote the paper and validation. MM: optimization of design and data collection. FA: generated the figures, writing manuscript. MR: data collection. MY: supervised and did the paper editing work.

Funding The study is supported by the ICT Division of the Ministry of Posts, Telecommunications and Information Technology, Dhaka, Bangladesh.

Availability of Data and Material Data and materials will be available upon request to the corresponding author.

Declarations

Ethics Approval Approved.

Consent to Participate Approved.

Consent for Publication Approved.

Conflict of Interest The authors declare no competing interests.

References

1. Homola J, Yee SS, Gauglitz G (1999) Surface plasmon resonance sensors: review. Sensors Actuators B Chem 54(1):3–15. https://doi.org/10.1016/S0925-4005(98)00321-9
2. Yanase Y, Hiragun T, Yanase T, Kawaguchi T, Ishii K, Hide M (2013) Application of SPR imaging sensor for detection of individual living cell reactions and clinical diagnosis of type I allergy. Allergol Int 62(2):163–169. https://doi.org/10.2332/allergolint.12-RA-0505
3. Mahmood AI, Ibrahim RK, Mahmood AI, Ibrahim ZK (2018) Design and simulation of surface plasmon resonance sensors for environmental monitoring. J Phys Conf Ser. https://doi.org/10.1088/1742-6596/1003/1/012118
4. Ramola A, Marwaha A, Singh S (2021) Design and investigation of a dedicated PCF SPR biosensor for CANCER exposure employing external sensing. Appl Phys A Mater Sci Process. https://doi.org/10.1007/s00339-021-04785-2
5. Lu J et al (2016) Fiber optic-SPR platform for fast and sensitive infliximab detection in serum of inflammatory bowel disease patients. Biosens Bioelectron 79:173–179. https://doi.org/10.1016/j.bios.2015.11.087
6. Krohn DA, MacDougall T, Mendez A (2014) Fiber optic sensors: fundamentals and applications. Bellingham, WA: Spie Press, pp 233–310
7. Rahman MM, Molla MA, Paul AK, Based MA, Rana MM, Anower MS (2020) Numerical investigation of a highly sensitive plasmonic refractive index sensor utilizing hexagonal lattice of photonic crystal fiber. Results Phys. 18:103313. https://doi.org/10.1016/j.rinp.2020.103313
8. Gupta BD, Verma RK (2009) Surface plasmon resonance-based fiber optic sensors: principle, probe designs, and some applications. J Sensors. https://doi.org/10.1155/2009/979761
9. Jorgenson RC, Yee SS (1993) A fiber-optic chemical sensor based on surface plasmon resonance. Sensors Actuators B Chem 12(3):213–220. https://doi.org/10.1016/0925-4005(93)80021-3
10. Islam A, Hasan A, Adnan A, Ullah A (2020) Novel SPR biosensor with Simple PCF structure of hexagonal lattice operating in Near-IR 2020. In 2nd Int Conf Adv Inf Commun Technol ICAICT, pp 382 386.https://doi.org/10.1109/ICAICT51780.2020.9333493
11. Hassani A, Skorobogatiy M (2006) Design of the microstructured optical fiber-based surface plasmon resonance sensors with enhanced microfluidics. Opt Express 14(24):11616. https://doi.org/10.1364/oe.14.011616
12. Islam MS, Islam MR, Sultana J, Dinovitser A, Ng BW-H, Abbott D (2019) Exposed-core localized surface plasmon resonance biosensor. J Opt Soc Am B 36(8):2306. https://doi.org/10.1364/josab.36.002306
13. Yang H, Wang G, Lu Y, Yao J (2021) Highly sensitive refractive index sensor based on SPR with silver and titanium dioxide coating. Opt Quantum Electron 53(6):1–13. https://doi.org/10.1007/s11082-021-02981-1
14. Shafkat A (2020) Analysis of a gold coated plasmonic sensor based on a duplex core photonic crystal fiber. Sens. Bio-Sensing Res. 28:100324. https://doi.org/10.1016/j.sbsr.2020.100324
15. Fu Y, Liu M, Shum P, Chu L (2020) An ultrahighly sensitive photonic crystal fiber based surface plasmon resonance sensor. Optik (Stuttg) 212:164649. https://doi.org/10.1016/j.ijleo.2020.164649
16. Rahman MM, Rana MM, Anower MS, Rahman MS, Paul AK (2020) Design and analysis of photonic crystal fiber-based plasmonic microbiosensor: an external sensing scheme. SN Appl Sci. https://doi.org/10.1007/s42452-020-2998-3
17. Hameed MFO, Alrayk YKA, Obayya SSA (2016) Self-calibration highly sensitive photonic crystal fiber biosensor. IEEE Photonics J 8(3):1–12. https://doi.org/10.1109/JPHOT.2016.2563319
18. Akter S, Rahman MZ, Mahmud S (2019) Highly sensitive open-channels based plasmonic biosensor in visible to near-infrared wavelength. Results Phys. https://doi.org/10.1016/j.rinp.2019.102328
19. Hossain MB, Riazul Islam SM, Hossain KMT, Abdulrazak LF, Sakib MN, Amiri IS (2020) High sensitivity hollow core circular shaped PCF surface plasmonic biosensor employing silver coat: a numerical design and analysis with external sensing approach. Results Phys. https://doi.org/10.1016/j.rinp.2019.102909
20. Wang H, Yan X, Li S, An G, Zhang X (2016) High sensitivity refractive index sensor based on dual-core photonic crystal fiber

with hexagonal lattice. Sensors (Switzerland). https://doi.org/10.3390/s16101655
21. Hasan MR, Akter S, Ahmed K, Abbott D (2018) Plasmonic refractive index sensor employing niobium nanofilm on photonic crystal fiber. IEEE Photonics Technol Lett 30(4):315–318. https://doi.org/10.1109/LPT.2017.2786475
22. Liu C et al (2018) Birefringent PCF-based SPR sensor for a broad range of low refractive index detection. IEEE Photonics Technol Lett 30(16):1471–1474. https://doi.org/10.1109/LPT.2018.2856859
23. Liu C et al (2018) Analysis of a surface plasmon resonance probe based on photonic crystal fibers for low refractive index detection. Plasmonics 13(3):779–784. https://doi.org/10.1007/s11468-017-0572-7
24. Islam MR, Khan MMI, Mehjabin F, Chowdhury JA, Islam M (2020) Design of a fabrication friendly & highly sensitive surface plasmon resonance-based photonic crystal fiber biosensor. Results Phys. 19:103501. https://doi.org/10.1016/j.rinp.2020.103501
25. Mahdiraji GA et al (2014) Challenges and solutions in fabrication of silica-based photonic crystal fibers: an experimental study. Fiber Integr Opt 33(1–2):85–104. https://doi.org/10.1080/01468030.2013.879680
26. Rifat AA, Haider F, Ahmed R, Mahdiraji GA, Mahamd Adikan FR, Miroshnichenko AE (2018) Highly sensitive selectively coated photonic crystal fiber-based plasmonic sensor. Opt Lett 43(4):891. https://doi.org/10.1364/ol.43.000891
27. Islam MR et al (2020) Design and analysis of birefringent SPR based PCF biosensor with ultra-high sensitivity and low loss. Optik (Stuttg). 221:165311. https://doi.org/10.1016/j.ijleo.2020.165311
28. Singh S, Prajapati YK (2019) Highly sensitive refractive index sensor based on D-shaped PCF with gold-graphene layers on the polished surface. Appl Phys A Mater Sci Process 125(6):1–7. https://doi.org/10.1007/s00339-019-2731-5
29. Al Mahfuz M, Hossain MA, Haque E, Hai NH, Namihira Y, Ahmed F (2020) Dual-core photonic crystal fiber-based plasmonic RI sensor in the visible to near-IR operating band. IEEE Sens J 20(14):7692–7700. https://doi.org/10.1109/JSEN.2020.2980327
30. Rifat AA, Hasan MR, Ahmed R, Butt H (2017) Photonic crystal fiber-based plasmonic biosensor with external sensing approach (erratum). J Nanophotonics 12(01):1. https://doi.org/10.1117/1.jnp.12.019901
31. Momota MR, Hasan MR (2018) Hollow-core silver coated photonic crystal fiber plasmonic sensor. Opt Mater (Amst) 76:287–294. https://doi.org/10.1016/j.optmat.2017.12.049
32. Hasan MR et al (2018) Spiral photonic crystal fiber-based dual-polarized surface plasmon resonance biosensor. IEEE Sens J 18(1):133–140. https://doi.org/10.1109/JSEN.2017.2769720
33. Luan N, Han H, Zhao L, Liu J, Yao J (2019) Opening up dual-core microstructured optical fiber-based plasmonic sensor with large detection range and linear sensitivity. Opt Mater Express 9(2):819. https://doi.org/10.1364/ome.9.000819
34. Baqir MA, Farmani A, Fatima T, Raza MR, Shaukat SF (2018) Nanoscale, tunable, and highly sensitive biosensor utilizing hyperbolic metamaterials in the near-infrared range. Appl Opt 57:9447–9454